Embedded Magnetism in $YBa_2Cu_3O_7$ Associated to Cu-O Vacancies within Nanoscale Intergrowths: Implications for Superconducting Current Performance

*Elena Bartolomé**[1], Bernat Mundet[2], Roger Guzmán[2], Jaume Gázquez[2], S. Manuel Valvidares[3], Javier Herrero-Martín[3], Eric Pellegrin[3,†], Teresa Puig[2], Xavier Obradors[2]*

1. Dep.Mechanical Engineering, Escola Universitària Salesiana de Sarrià (EUSS), Passeig Joan Bosco, 74; 08017 Barcelona, Spain. E-mail: ebartolome@euss.es

2. Institut de Ciència de Materials de Barcelona (ICMAB), Consejo Superior de Investigaciones Científicas (CSIC), Campus UAB, 08193 Bellaterra, Barcelona, Spain

3. ALBA Synchrotron Light Source; 08290 Cerdanyola del Vallès, Barcelona, Spain

KEYWORDS. Nanocomposites, magnetic nanodefects, YBCO thin-films, high T_c superconductors, vacancies

ABSTRACT. Stacking faults are ubiquitous structural defects in $YBa_2Cu_3O_7$ high T_c superconductors. Far from being detrimental, the control of the defect landscape, i.e. the length,

density and distribution of $YBa_2Cu_4O_y$ (Y124) intergrowths, changing the nanostrain of the material can be used to enhance the vortex pinning properties of the superconductor, as required for applications. Recently, the use of advanced scanning transmission electronic microscopy has unveiled the presence of complex point nanodefects (clusters of Cu and O vacancies) within Y124, with an associated magnetic moment predicted by density functional calculations. In this work, we investigate the nature of defect-driven embedded magnetism in YBCO samples (thin-films, nanocomposites and a single-crystal) containing different distributions of Y124 intergrowths using X-ray magnetic circular dichroism (XMCD), combined with scanning transmission electron microscopy (STEM) and electron energy loss spectroscopy (EELS). The dichroic Cu signal correlates with the density of Y124 intergrowths, demonstrating the defect-driven origin of the embedded magnetism. Remarkably, a Cu XMCD signal is observed even in the single-crystal, associated to the small presence of defects at the surface. Our work thus demonstrates the ubiquity of embedded magnetism in YBCO associated to faulted Y124 defects.

INTRODUCTION

In high-temperature superconductor $YBa_2Cu_3O_7$ (YBCO), the ultimate current performance, under the high fields and temperatures required for power applications, is determined by the ability of the material to pin flux vortices in nanodefects of a dimension of the superconductor coherence length, $\xi_c \approx 1$ nm.[1–6] Accordingly, tremendous efforts have been made in recent years towards nanoengineering the defect landscape of YBCO films.[7–12] The most common and widespread structural defect in YBCO samples is the $YBa_2Cu_4O_8$ (Y124) intergrowth, basically consisting of two CuO chain layers within the YBCO matrix (**Figure 1**). Y124 intergrowths inevitably appear in YBCO thin-films grown by different methods, both physical and chemical,

especially at surfaces and interfaces. For chemical solution deposition (CSD) thin-films[13], we have shown that the artificial inclusion of secondary phases notably modifies the Y124 landscape.[14,15]

Recently, the use of advanced Scanning Transmission Electron Microscopy (STEM) techniques has allowed us to unveil previously overlooked nanodefects buried in YBCO, which lead to surprising changes in the electronic and magnetic properties of the material. Indeed, aberration-corrected STEM imaging allowed us to observe the presence of complex point defects, consisting of Cu and O vacancies, within Y124 intergrowths in YBCO thin-films.[16] The formation of these O-decorated Cu-vacancies is required to counterbalance the off-stoichiometry associated to the generation of Y124 intergrowths. The defect cluster $2V_{Cu}+3V_O$, see **Figure 1b**, was shown to be the most energetically stable type of defect by Density Functional Theory (DFT) calculations, especially at the conditions under which YBCO films are grown and thus where these Y124 intrergrowths form. Remarkably, the DFT calculations also predicted a magnetic moment of ≈2.2 μ_B per $2V_{Cu}+3V_O$ defect cluster (of which ≈1.3 μ_B associated to the four Cu atoms neighboring the defect). In-field X-ray Magnetic Circular Dichroism (XMCD) measurements[17] at the Cu $L_{2,3}$ edge were performed in Total Electron Yield (TEY) surface-sensitive mode on YBCO thin-films and YBCO nanocomposites, exhibiting a large density of Y124 intergrowths at the surface layers. Both samples displayed a XMCD(B) superparamagnetic signal, even below the superconducting temperature T_c, which was assigned to the presence of a dilute system of ferromagnetic $2V_{Cu}+3V_O$ clusters embedded in YBCO.[16]

We note here that the presence of out-of-plane Cu magnetic moments in YBCO has been also reported in YBCO/LSMO heteroestructures, although in that case the moment is induced in the superconductor by the Mn layer.[5] Besides, previous dichroism experiments in YBCO, La_{2-}

$_xSr_xCuO_4$, and $Nd_{1.2}Ba_{1.8}Cu_3O_{7-x}$ thin-films and single crystals have shown the development of field-induced magnetic moments in both the normal and superconducting states.[18] There, the observed dichroic signal, linear with the magnetic field, was interpreted to arise from action of the Dzyaloshinskii-Moriya (DM) interaction with the CuO_2 planes, leading to an out-of-plane spin canting component, as also observed in the LSCO/LSMO interfaces. However, the lack of details on the nanoscale structure of these samples did not allow discarding this moment to be, at least partially, driven by defects.

In this paper, we study in depth the nature of embedded magnetism in YBCO associated to defects through the study of thin-films (pristine and nanocomposites) containing different concentration and distribution of Y124 defects with vacancy clusters. It will be shown that in all cases, the magnitude of the dichroic Cu signal correlates with the density of Y124 intergrowths, demonstrating a defect-driven origin of the embedded magnetism. Remarkably, a Cu XMCD signal is observed even in the YBCO single-crystal, associated with $2V_{Cu}+3V_O$ clusters, due to the presence of Y124 intergrowths at the surface. Our work thus demonstrates the ubiquity of magnetism in YBCO associated to nanofaulted Y124, and underlies the importance of a careful examination of the defect nanostructure in the study of the origin of magnetism in superconducting samples and heterostructures. We discuss the implications of our findings for the potential enhancement of current performance for superconducting power applications.

RESULTS AND DISCUSSION

In this work, YBCO samples with a different density and distribution of Y124 intergrowths have been considered, as shown by the STEM Z-contrast images in **Figure 2**:

(a) A standard 250 nm-thick YBCO film grown on top of a 5x5 mm^2 (100) LAO substrate by the CSD method[13] (**Figure 2a**). These type of samples present numerous and relatively long (~100-

150 nm) Y124 intergrowths at the surface, but the density of defects decreases abruptly in the interior (bulk) of the film. Stacking faults (SF's) are ordered and flat (**Figure 2d**).

(b) A 5x5 mm^2, 250 nm-thick YBCO/LAO nanocomposite (NC) including a 10 % molar percentage of Ba_2YTaO_6 (BYTO) secondary phases.[19] The inclusion of secondary nanoparticles, of size ~10-30 nm, induces a high density of Y124 intergrowths distributed throughout the whole YBCO thickness (**Figure 2b**). From the STEM images, the length and number of intergrowths generated in the YBCO matrix could be quantified. The obtained histograms evidence that the concentration of short Y124 intergrowths (length <50 nm) is enhanced with respect to pristine films, where only a smaller number of long intergrowths (length >150 nm), principally located at the surface are formed[14]; NCs grown using an extremely fast, flux-heating process present an even higher population of shorter (<20 nm) SF's.[20] The SF's induced in the NC by the presence of nanoparticles appear extremely rippled (**Figure 2e**). We analyzed as well a second YBCO+10% BYTO NC, with a similar intergrowth population, but des-oxygenated after growth, noted NC(des-ox), so as to analyze the effects on defect-driven embedded magnetism. The pristine YBCO film and NC samples presented good superconducting characteristics with critical temperature T_c=91 K and critical current densities $J_c \approx 4$ MA/cm^2 in self-field at 77 K.

(c) A 0.5x0.5 mm^2, 30 μm-thick YBCO single-crystal (SC) grown by the flux-growth technique[21]. The sample shows some Y124 intergrowths at the surface, as shown in **Figure 2c** and zoomed area **Figure 2f**.

YBCO thin-film. So as to prove the correlation between the Cu XMCD signal and the amount of $2V_{Cu}+3V_O$ defects, we measured a TFA-grown YBCO film (with a much higher density of

intergrowths in the sample surface than within the matrix), in TEY surface-sensitive and FY-bulk sensitive modes simultaneously (see schematics in **Figure 3**).

Measurements were carried out at T=1.6 K, under an applied field B=6 T parallel to the beam, in grazing incidence $\theta^{*}\approx 55^{o}$ (the "magic angle" was chosen so as to enable FY detection, on the one hand, and cancel the dipolar magnetic moment contribution T_z, on the other). **Figure 3a-b** shows a comparison between the XAS & XMCD spectra obtained in TEY and FY modes. The spectra in TEY mode are similar to those earlier reported by us for a different YBCO thin-film[16], confirming the reproducibility of the effect. Regarding results in FY, it has to be noted that self-absorption effects in this detection mode become important, due to the longer penetration depth of the X-rays. Therefore, the as- measured XAS spectra were corrected for self-absorption, according to the following experimental procedure, proposed by de Groot[22], and similar to that described by Cuartero *et al.*[23], as follows. The experimental fluorescence absorption μ_F can be expressed as [24]:

$$\mu_F(E) = \frac{\left(\frac{\Omega}{4\pi}\right)\varepsilon_f \mu(E)}{\mu_T(E) + \mu_T(E_F)\frac{\sin\theta}{\sin\varphi}}, \qquad (1)$$

where $\mu_T(E)$ is the total absorption coefficient, which includes contributions from the edge of interest and from other edges of all atoms in the compound [$\mu(E)$+$\mu_{bkg}(E)$]; $\mu_T(E_F)$ is the total absorption coefficient at the energy of the fluorescence photons; $E_{F.}$ θ and φ are the angles between the sample surface and the direction of the incoming and the detected fluorescence photons, respectively; ($\Omega/4\pi$) is the solid angle covered by the detector, and ε_f is the fluorescence yield of the absorber atom. Since the energy range at the Cu $L_{2,3}$ is small, $\mu_T(E)$ can be approximated to $\mu_T(E)\approx\mu(E)$+k, where k is constant.

Considering Equation (1) and grouping the constant factors, the absorption coefficient without self-absorption effects, can be rewritten as:

$$\mu(E) = \frac{C_1 \mu_F(E)}{C_2 - \mu_F(E)} = \mu_{TEY}(E) - \mu_{bkg}(E). \quad (2)$$

Hence, the TEY-detected (background subtracted) μ^+ and μ^- experimental spectra were fitted to the corresponding $\mu_F(E)$ measurement to find the C_1 and C_2 constants. Then, Equation (2) was applied to the as-measured FY spectra to finally obtain the self-absorption corrected $\mu(E)$ spectra. The XMCD was determined as the difference between the self-absorption corrected μ^- - μ^+. The comparison between the as-measured μ_F (dotted line) and the final μ (thick line) after the saturation correction is shown in **Figure 3b**. Note that the correction method is based upon the fact that, despite spectral differences are expected between the FY and TEY spectra, associated with the different defect composition or oxygenation of the sample surface compared to the bulk, the L_2 to L_3 ratio should not change. We estimate the error of this procedure is ~10%, which is within the total experimental uncertainty. Once the absorption correction is done, the FY can be adequately compared with the TEY spectra. The percentage Cu XMCD signal measured by FY (bulk) is about 2.6±0.2% of the white line, significantly smaller than the signal measured by TEY on the sample surface (8.6±0.8%). This result demonstrates that a larger embedded Cu magnetic signal is found in regions with more abundance of cluster defects in YBCO.

Furthermore, the sum rules were applied in order to determine the orbital (m_L), effective ($m_{s,eff}$) and total (m_{TOT}) magnetic moments at the surface and interior of the YBCO thin-film. **Table 1** summarizes the results obtained from the TEY and FY spectra. (Note that the effective magnetic moment is the sum of the spin and dipolar contributions, $m_s^{eff}=m_s+m_T$, but since measurements were performed at the "magic angle" $\theta^*=55^o$ such that $m_T=0$, $m_s^{eff}\equiv m_s$, the total

magnetic moment could be directly determined, as $m_{TOT} = m_s + m_L$, see below). The results evidence that the total magnetic moment m_{TOT}(TEY) from the surface is 70% larger than in the bulk, m_{TOT}(FY). In our previous work, we reported variations in the TEY-determined m_{TOT} of about 20% within a sample, points (1)-(2)-(3) in the schematics shown in **Figure 3**, assigned to local changes in the concentration of point defects at the surface.[16] The present experiment evidences a more radical decrease in the Cu magnetic moment when the density of defects tends to zero.

We turn now our attention to the spectroscopic differences observed between the XAS measured in TEY and FY. The XAS(TEY) exhibits "satellite" above L_3 at 936.5 eV (signaled by the arrow in **Figure 3a**) not present in the XAS(FY) spectrum, in which only a "shoulder" next to L_3 appears. The satellite peak owes mainly to the spectral contribution of Cu^{1+} in the CuO chains[25], therefore, its larger intensity in the TEY-determined XAS is an indication of the higher abundance of Y124 intergrowths in the sample surface. However, XAS measurements are not ideal to distinguish between chain and plane contributions, because the spectra arise from the integrated contribution of all Cu in the sample.

In order to get more insight into the electronic changes induced by the Y124 intergrowths, we studied the EELS Cu L edge fine structure. EEL spectrum imaging allows for simultaneously acquiring an Annular Dark Field image with an associated EEL spectrum for each and every pixel of the image, which permits visualizing spectral changes within a STEM Z-contrast image.[26] Therefore, it is possible to obtain separately the Cu L edge spectra at specific chain or plane positions, see **Figure 4a**. **Figure 4b** compares the Cu L edges obtained at CuO chains (red line) and plane CuO_2 (blue line) positions within the YBCO lattice. The spectra are similar to those earlier reported by N. Gauquelin *et al.*[25] for an $YBCO_7$ single-crystal. The Cu L_3

peak acquired at the chains splits into the α (931.5 eV) and β (934 eV) peaks, and it shifts towards higher energies when the oxidation state of the Cu decreases. The splitting of the L_3 in the single-chain layers stems from a mixture of Cu^{1+}/Cu^{2+} cations, as the α peak is associated to a Cu^{2+} and β to Cu^{1+}. On the other hand, Cu cations in the CuO_2 planes show a Cu L_3 peak associated mainly a Cu^{2+} signal.[27] In addition, **Figure 4c** shows the Cu L edge spectra obtained at double-chains of several Y124 intergrowths, compared with the spectrum at a single-chain of YBCO (orange line). A decrease in the α/β ratio is observed in the spectrum measured at double-chains. This is in turn related to the oxygen concentration of the YBCO structure, as the O^{2-} anions located at the chain layers take electrons from their neighboring Cu cations, thus changing their valence from Cu^{1+} to Cu^{2+}.[25,28–30] Therefore, the presence of oxygen vacancies that escort the Cu vacancies found within the Y124 intergrowths render the opposite result, i.e., a higher concentration of Cu^{1+} in the double CuO chains and a lower α/β ratio. Wrapping up, the relative increase of the β peak is coherent with the "satellite" peak in the XAS spectrum discussed above. This finding actually correlates well with recent results on the superconducting properties of ultrathin YBCO films having a high concentration of Y124[31]: it has been concluded that defective Y124 intergrowths quench the superconducting behavior, an issue that should be expected if the Cu valence is reduced.

Nanocomposites. We investigated, for comparison with the YBCO thin-film, the presence of embedded magnetism in a nanocomposite film showing a more homogeneous distribution of Y124 intergrowths through the thickness (**Figure 2b**). **Figure 5a, b** (left) shows the XAS & XMCD at the Cu $L_{2,3}$ edge measured by TEY (surface) and FY (bulk) for this sample. FY XAS spectra were corrected for self-absorption, following the procedure described in the previous section. Several conclusions can be drawn.

It is first noted that the dichroic signal at the surface in the NC (2.5±0.2%) is smaller than in the thin-film (8.6±0.8%), confirming previous evidence obtained for different NCs.[32] This experimental observation shows that in NCs, where SF's are strongly rippled (**Figure 2e**) in comparison with the flat SF's found in YBCO films (**Figure 2d**), the presence of nanostrains produces local changes in the structure, which reduce the formation of magnetically 'effective' defect clusters.

On the other hand, the dichroic signal measured by FY at the interior of the sample (1.2±0.2%) is close to the value at the surface, in agreement with the more homogeneous distribution of Y124 intergrowths in the NC, as compared with the thin-film. The slight decrease in the XMCD, and the absence of a clear "satellite" in the XAS spectrum measured by FY seems to indicate that, despite the density of SF's is similar to the surface, not all the defect clusters contribute equally to the XMCD signal, which might be due to the strained regions found within the NC's film, and therefore the deformation of both the YBCO matrix and the Y124 intergrowths.[15]

Overall the above results indicate that the observation of defect-driven embedded magnetism requires, first, necessarily the presence Y124 intergrowths, but also a structure resembling that predicted by the DFT calculations in which O-decorated Cu vacancies ($2V_{Cu}+3V_O$) are formed. Any lattice distortion may affect the structure and even the stoichiometry of the faulted YBCO, yielding to a lower concentration of 'active' ferromagnetic clusters.

A possible approach to vary the number of vacancies, for a given Y124 distribution, is to des-oxygenate the sample. Therefore, in the next experiment we measured the XAS & XMCD at

the Cu $L_{2,3}$ edge, at the surface and bulk, of a des-oxygenated NC (**Figure 5a, b, right**). The XAS spectrum at the O K edge measured in FY for NC(ox) and NC(des-ox) reflects the different oxygenation of the two studied samples (**Figure 5c**): for the NC(ox) an intense pre-peak at 528.55 eV is observed as expected in well-oxygenated YBCO samples[25], while this pre-peak is much weaker and shifted to higher energies in the des-oxygenated one.

The results at the Cu edge evidence a small increase in the dichroic signal for the des-oxygenated NC. We had observed a similar result for oxygenated/des-oxygenated hybrid CFO-YBCO NCs.[32] In particular, the dichroic signal measured at the interior of the NC is larger (2.9±0.2%), and now comparable to the signal in the surface (3.2±0.2%), and the XAS spectrum has developed the characteristic "satellite", close to L_3. The latter is in agreement with recent results showing that upon des-oxygenating YBCO, vacancies are preferably formed in CuO chains and double-chains rather than in BaO planes [*submitted*]. Our results indicate that the des-oxygenation process helps the creation of oxygen vacancies within the structure of intergrowths, increasing the level of embedded magnetism. More investigation is envisaged to systematically analyze the effect of oxygen dosing on the presence of magnetic defects in Y124.

Single-crystal. The STEM analysis of our single-crystal reveals the existence of a high concentration of Y124 intergrowths at the surface (see **Figure 2c**). In spite of the fact that according to DFT calculations, the formation of Cu vacancies, and therefore the defect cluster $2V_{Cu}+3V_O$ within Y124 intergrowths, is more favorable under the low oxygen pressures used to grow the YBCO thin-films than under the much higher oxygen pressures utilized for the growth of SC's, these complex defects do appear. Indeed, **Figure 6a** shows a high magnification Z-contrast image of the surface of the single crystal featuring a high concentration of Y124 intergrowths, easily identified by their double Cu layer. These double Cu layers also present a

dimmer intensity, which is associated to the presence of Cu vacancies within the Y124 intergrowths (marked in yellow). Interestingly, the Cu XMCD measurement in TEY (surface) mode of this sample presents a robust (5%) dichroic signal, **Figure 6b.** The result proves that whenever the Y124 intergrowths are present in YBCO, there are point vacancies buried in them, and as a result a net magnetic moment of the Cu atoms surrounding them. Researchers investigating the magnetic properties of superconducting/ferromagnetic heterostructures should be aware of this result, as the presence of these type of complex-vacancies at interfaces, even in very well controlled growth conditions, often occurs.[33–37]

Angular dependence. In order to gain insight into the anisotropic characteristics of the defect-driven moments, we performed XAS & XMCD measurements as a function of the beam incident angle, in TEY mode. We recall here that the effective spin moment, m_s^{eff}, is angular dependent: it relates the isotropic spin (m_s) moment and the anisotropic intra-atomic spin dipole moment (m_T). The latter expresses the inhomogeneous spatial distribution of the spin density over the atomic unit cell, due to the anisotropic charge distribution arising from strongly directional bonds or crystal field.[38] As extensively discussed in[39,40], the m_T term in Cu^{2+} sites with high anisotropy may be non-negligible.

The sum rules[41,42], corrected for angular effects, were applied to evaluate the Cu orbital and effective spin moments:

$$m_L(\theta) = -2n_h \frac{q(\theta)}{I^{ISO}} \quad (3)$$

$$m_S^{eff}(\theta) = -3n_h \frac{\left[3p(\theta) - 2q(\theta)\right]}{I^{ISO}} \quad (4)$$

where n_h is the number of holes in the 3d shell, which we assumed to be n_h=1 for Cu^{2+} sites ($3d^9$). The integrals $p(\theta)$, $q(\theta)$ and $r(\theta)$ are defined as:

$$q(\theta) = \int_{L_{2,3}} I^{-}(E,\theta) - I^{+}(E,\theta)dE \quad (5)$$

$$p(\theta) = \int_{L_3} I^{-}(E,\theta) - I^{+}(E,\theta)dE\,, \quad (6)$$

$$I^{ISO} = \int_{L_{2,3}} I^{-}(E,\theta) + I^{+}(E,\theta) + I^{0}(E)dE\,, \quad (7)$$

where $I^0(E)$ is the isotropic absorption intensity measured with the photon linear polarization vector perpendicular to the direction of the incident light. Since $I^0(E)$ is difficult to determine, it is often approximated as $I^0(E) = \left(I^{-}(E,\theta) + I^{+}(E,\theta)\right)/2$, which can lead to large errors for very anisotropic environments. The alternative, proposed by Stepanow *et al.*[39], is to experimentally determine I^{ISO} as:

$$I^{ISO} = \int_{L_{2,3}} \frac{I^{-}(E,\theta) + I^{+}(E,\theta)}{f(\theta)}dE \quad (8)$$

where $f(\theta)$ is a function describing the angular dependence of the integrated XAS(θ) whiteline.

As shown in **Figure 7a**, a strong XAS angular dependence was found for Cu atoms in YBCO thin-films. The L_2+L_3 XAS integral decreases according to the function $f(\theta) = \left(\cos^2\theta - 1\right)/2$ predicted for orbitals having a C_4 axis perpendicular to the surface[43,44] (**Figure 7b**, red symbols). Notably, a smoother dependence was found for Cu atoms in the NC(ox) sample (**Figure 7b**, green symbols). Phenomenologically, this behavior is expected when orbitals are canted, forming an angle $\gamma<90^o$ with respect to the substrate[43]: $f(\theta) = (2/3)\left[1 - 0.25(3\cos^2\theta - 1)(3\cos^2\gamma - 1)\right]$; in this case we estimate $\gamma\approx60^o$. This result might be related to the strongly rippled Y124 intergrowths found in the NCs.

The angular-corrected sum rules Equations (3-4) were applied to determine $m_L(\theta)$, $m_s^{eff}(\theta)$ moments, and the ratio $m_L/m_s^{eff}(\theta)$. **Figure 7c, d** shows the results obtained for the YBCO thin-film. We adopted the methodology[45], previously applied to highly-anisotropic atoms on surfaces[46,47], to evaluate the *x*,*y* and *z* components of the Cu moments. The angular dependence of the orbital and the effective magnetic moments can be, respectively, decomposed as:

$$m_L(\theta) = m_L^z \cos^2\theta + m_L^{xy} \sin^2\theta \quad (9)$$

$$m_s^{eff}(\theta) = m_S - 7m_T^z\left[\cos^2\theta - (1/2)\sin^2\theta\right] \quad (10)$$

At the magic angle (θ^*=54.7°), the second term in Equation (10) cancels and thus $m_s^{eff}(\theta^*)$ provides directly m_s.[38] As shown in **Figure 7c, d** the $m_L(\theta)$, $m_s^{eff}(\theta)$ and $m_L/m_s^{eff}(\theta)$ experimental data could be simultaneously well fitted using Equations (8)-(9) with the four adjustable parameters collected in the inset. The spin moment value from the fitting, m_s=0.064±0.005 μ_B, agrees within the error with the direct measurement of m_s at the magic angle (0.061 μ_B). The orbital moment shows a small anisotropy, $m_L^z/m_L^{xy}\approx$1.4, compared e.g. with values reported for Cu in organometallic molecules grafted onto substrates.[39,48] The orbital-to-effective spin moment ratio, practically angle-independent, is $m_L/\ m_s^{eff}\approx$0.22, close to the value predicted from atomic model calculations for Cu^{2+} with a x^2-y^2 ground state.[40] The total magnetic moment at a given incidence angle is $m_{TOT}(\theta)=m_L(\theta)+\ m_s$, where it is found that m_s amounts ≈80% (90%) of in normal incidence for the YBCO thin-film (NC), respectively.

Field dependence. So as to study the field dependence of defect-driven moments, we measured the XMCD intensity versus applied field *B* for the NC(ox) and NC(des-ox) and the YBCO thin-film[16] at *T*=1.6 K for x-ray beam in normal incidence and using TEY detection. **Figure 8**

summarizes the $m_{TOT}(B)$ curves obtained for the three analyzed samples. The curves were obtained either recording full energy XMCD(B) spectra and applying the sum rules to determine $m_{TOT}(B)=m_S+m_L(B)$, or following the evolution of the Cu L_3 XMCD peak between -6 to 6 T, and then scaling the plot to the m_{TOT}(6T) value derived from the XMCD(6T) scan.

In the three samples, $m_{TOT}(B)$ deviates from linearity and tends to saturate at high fields. It can be fitted within the previously proposed model of superparamagnetic clusters including ferromagnetically ordered moments, with a Langevin curve, $m_{TOT}^{exp}(B) \approx \mu_s \cdot \mathcal{L}(\mu_c)$, where the saturation value μ_s corresponds to the total magnetic moment per average Cu in the sample, while μ_c gives the magnetic moment of each individual cluster.[16] The fitting parameters for the three samples are summarized in **Figure 8** (caption).

A question may arise of whether the type of complex clusters created in the three types of samples are similar, and the differences in the curves are solely related to a different density of existing defects. The inset of **Figure 8** shows that all the curves collapse when normalized to a common saturation value, indicating that the moment associated to a defect is approximately the same in every sample, $\mu_c=1.18\mu_B\pm0.20\ \mu_0$. Therefore, differences in μ_s values between samples are associated to different concentrations of complex point defects ($2V_{Cu}+3V_O$).

CONCLUSIONS

We have investigated the presence of Cu magnetism in YBCO samples of different types, including different distributions of Y124 intergrowths and thus the associated Cu-O vacancies. We have demonstrated the ubiquity of embedded superparamagnetism associated to the vacancy defect clusters, observed in YBCO thin-films, nanocomposites and even single-crystals, where Y124 often appears at the surface.

XMCD at the Cu edge performed simultaneously in TEY and FY detection modes on an YBCO thin-film, exhibiting a much larger concentration of Y124 at the surface, have allowed us to demonstrate the correlation between the Cu dichroic signal and the density of the defects' clusters within Y124 intergrowths.

All the nanocomposites investigated present a smaller magnetic dichroic signal than the pristine films, which is attributed to a smaller efficiency in the creation of effective magnetic cluster vacancies within the strained, rippled Y124 intergrowths induced by the presence of nanoparticles. A relatively smaller difference between the dichroic signals measured at the surface and the interior of the sample is observed for the NC, in agreement with the more homogeneous distribution of the defects' clusters within the Y124 intergrowths. Des-oxygenation of the NC has been found to favor the creation of O vacancy defects within Y124, especially within the bulk, slightly increasing the dichroic signal.

Angle-dependent XMCD measurements allowed us to characterize the orbital and effective spin magnetic moments, $m_L(\theta)$, $m_s^{eff}(\theta)$, of Cu in the vacancy clusters at T=1.6 K, B=6 T. The isotropic spin moment, m_s=0.064 μ_B, amounts 80% (90%) of m_s^{eff} for the YBCO film (NC), respectively, in normal incidence. A superparamagnetic $m_{TOT}(B)$ curve, associated to the presence of the copper-oxygen vacancy defects with a cluster ferromagnetic moment, is found both for the YBCO film and NCs.

The control over the nanostructure of YBCO is the key factor towards increasing vortex pinning, and thus the discovery of vacancy cluster defects with a magnetic moment even below the critical temperature of the superconductor, represents an opportunity to enhance the critical current performance of superconductors for applications. In recent years, the relative

contribution of the different types of pinning defects (isotropic and anisotropic, weak and strong) to the total critical current density in the different regions of the superconductor *H-T* phase diagram could be determined. The isotropic-weak pinning contribution, essentially associated to the presence of 0D point defects, is dominant in the low temperature (<20 K) region of the phase diagram at all fields, and thus the controlled addition of Cu-O vacancy clusters would be beneficial. Indeed, recent investigation of CSD-grown NCs have shown that in YBCO films where the addition of preformed nanoparticles led to short SF's and a large density of partial dislocations, a larger isotropic-weak contribution is observed (together with a larger isotropic-strong contribution associated to increased nanostrain pinning)[6], which may be possibly related to presence of abundant Cu-O cluster vacancies hosted by Y124 intergrowths. The ability to increase the current performance of by Cu-O vacancy addition would be particularly interesting for YBCO-based coated conductors for applications operating at low temperatures and high magnetic fields, e.g. magnets for accelerators, fusion, medical systems (NMR) etc.

METHODS

STEM-EELS: Scanning transmission electron microscopy observations were carried out in an aberration-corrected FEI Titan 60–300 microscope operated at 300 kV, fitted with a high-brightness field-emission gun (X-FEG) and a CEOS probe Cs corrector. All STEM images were acquired in High Angular Annular Dark Field (HAADF) imaging mode, in which the contrast scales with the atomic number Z (Z-contrast imaging).[49]

EELS were acquired with a NION UltraSTEM operated at 100 kV equipped with a NION aberration corrector and an EEL GATAN Enfina spectrometer. The statistical noise associated to each EEL spectrum was reduced by summing several spectra associated to equivalent crystal positions and by using the MSA (weighted PCA) plug-in that runs in the digital micrograph

software. All thin films for STEM were prepared by conventional methods, by grinding, dimpling, and Ar ion milling, whereas the STEM specimen of the single crystal was prepared with a Dual Helios Nanolab Focus Ion Beam.

XAS & XMCD: X-ray magnetic circular dichroism (XMCD) is an element and edge-selective technique, which has proved extremely versatile to investigate the magnetic properties of atoms in many different systems[17]. Soft X-ray absorption spectroscopy (XAS) and XMCD experiments of this work were carried on at ALBA Synchrotron light source (BOREAS beamline) in Barcelona. Total Electron Yield (TEY) surface-sensitive[50] and Fluorescence Yield (FY) bulk-sensitive detection modes were used. Measurements at the Cu $L_{2,3}$ edges were performed with the sample forming different angles (θ=0-70^{o}) with respect to the incident beam, at temperature T=1.6 K, and magnetic fields from -6 T to 6 T applied parallel to the photon beam. For the SC measurements could be done only in normal incidence, given the small size of the crystal. The beam polarization was changed between approximately 100% right (C^{+}) and left (C^{-}) circular polarization.

FIGURES

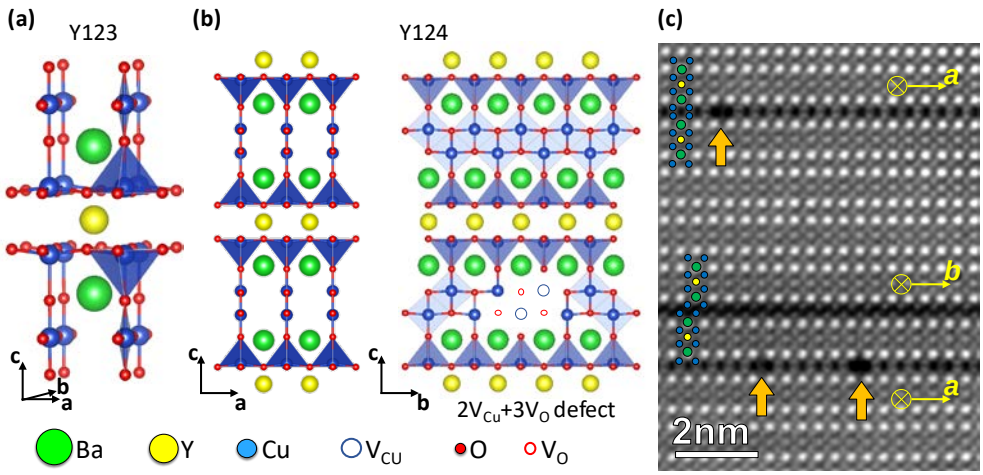

Figure 1. (a) YBCO (Y123) phase crystal structure (along [100]); (b) Y124 phase crystal structure (along [100] and [010] orientations); the formation of the complex-defect $2V_{Cu}+3V_O$ within the double-chain layer is shown; (c) atomic resolution image of the Y123 lattice with three Y124 intergrowths imaged along both the [010] and [100] orientation. The arrows signal the position of complex vacancies within Y124 intergrowths.

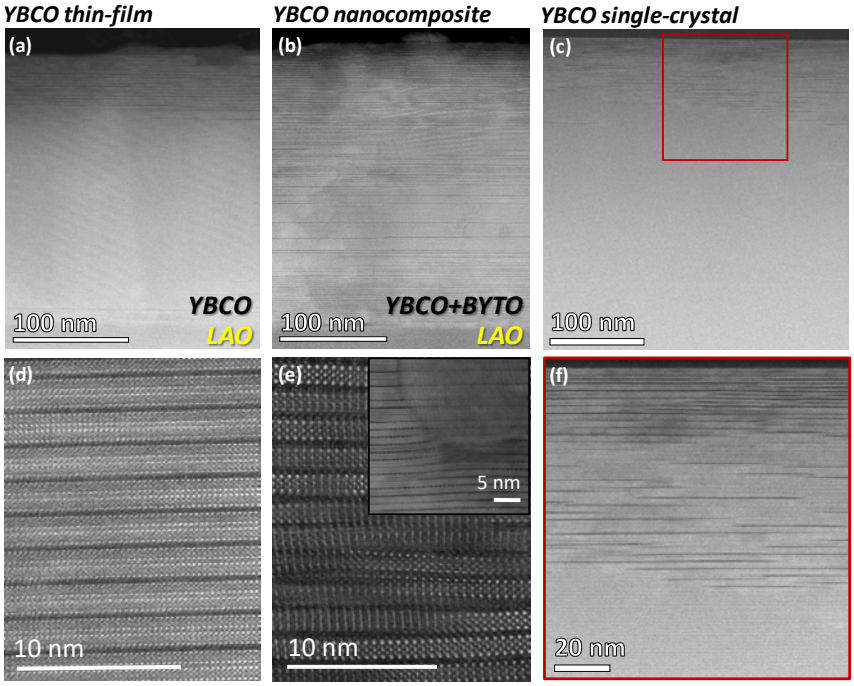

Figure 2. STEM Z-contrast images of (a) a CSD-grown YBCO thin-film, (b) a YBCO+10 % BYTO nanocomposite, and (c) an YBCO single-crystal, showing a different density and distribution of Y124 intergrowths; (d) Flat SF's in YBCO film, and (e) strongly rippled SF's in a NC, induced by the nanoparticles (inset); (f) Y124 intergrowths in the top layers of the SC.

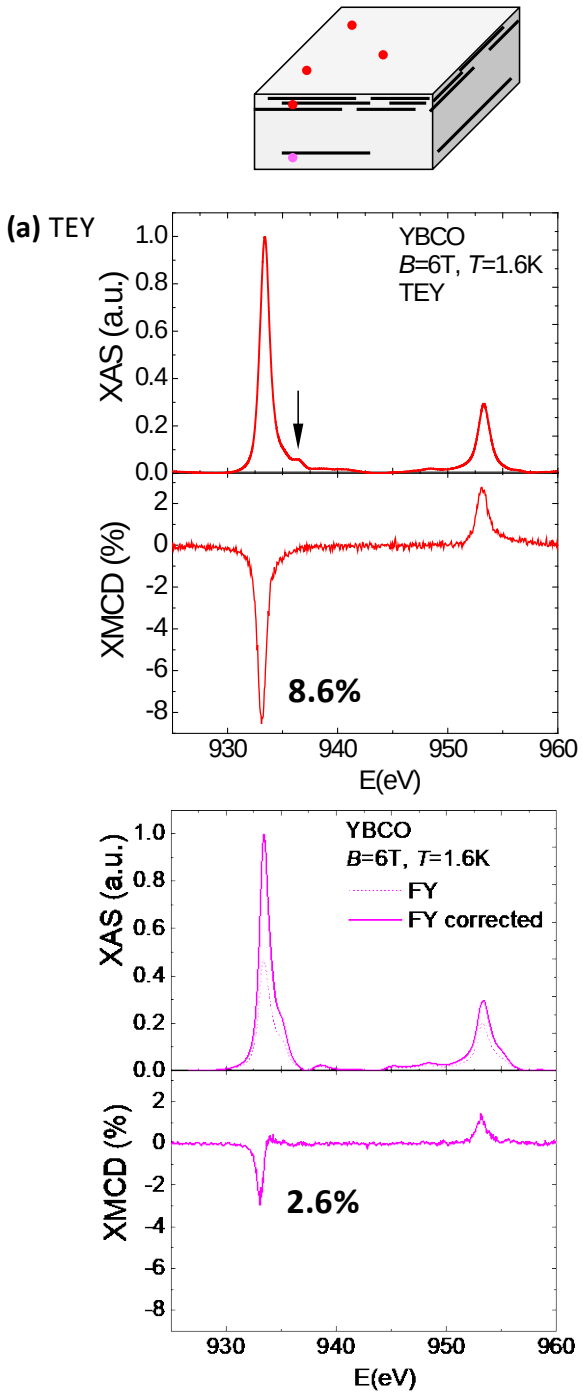

Figure 3. XAS & XMCD spectra for a TFA-grown YBCO thin-film with a larger density of Y124 intergrowths at the surface measured simultaneously in (a) TEY surface-sensitive mode and (b) FY bulk-sensitive mode, at T=1.6 K, B=6 T and beam incidence angle θ^*=55^o (see top schematics). In FY mode, the as-measured absorption spectrum (thin line) and self-absorption corrected spectrum (thick line) are shown.

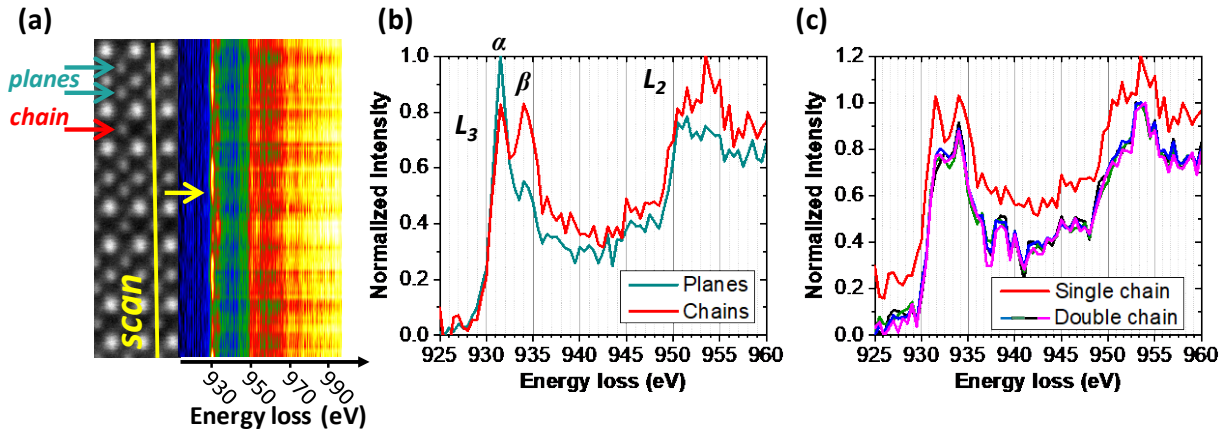

Figure 4. (a) Z-contrast image of the YBCO crystal together with Cu L edge spectra acquired vertically along the yellow line in the image. The intensity of the spectra is represented with a color scale. The superconducting planes and the single-chain layers are indicated with the blue and red arrows, respectively; (b) Obtained Cu L edge spectra for YBCO obtained at the planes (blue) and single-chain (red) positions; (c) Cu L edge at a single-chain in YBCO (orange line, shifted upwards for the sake of comparison), and several spectra obtained at double-chains of different Y124 intergrowths. Measurements were performed at room temperature.

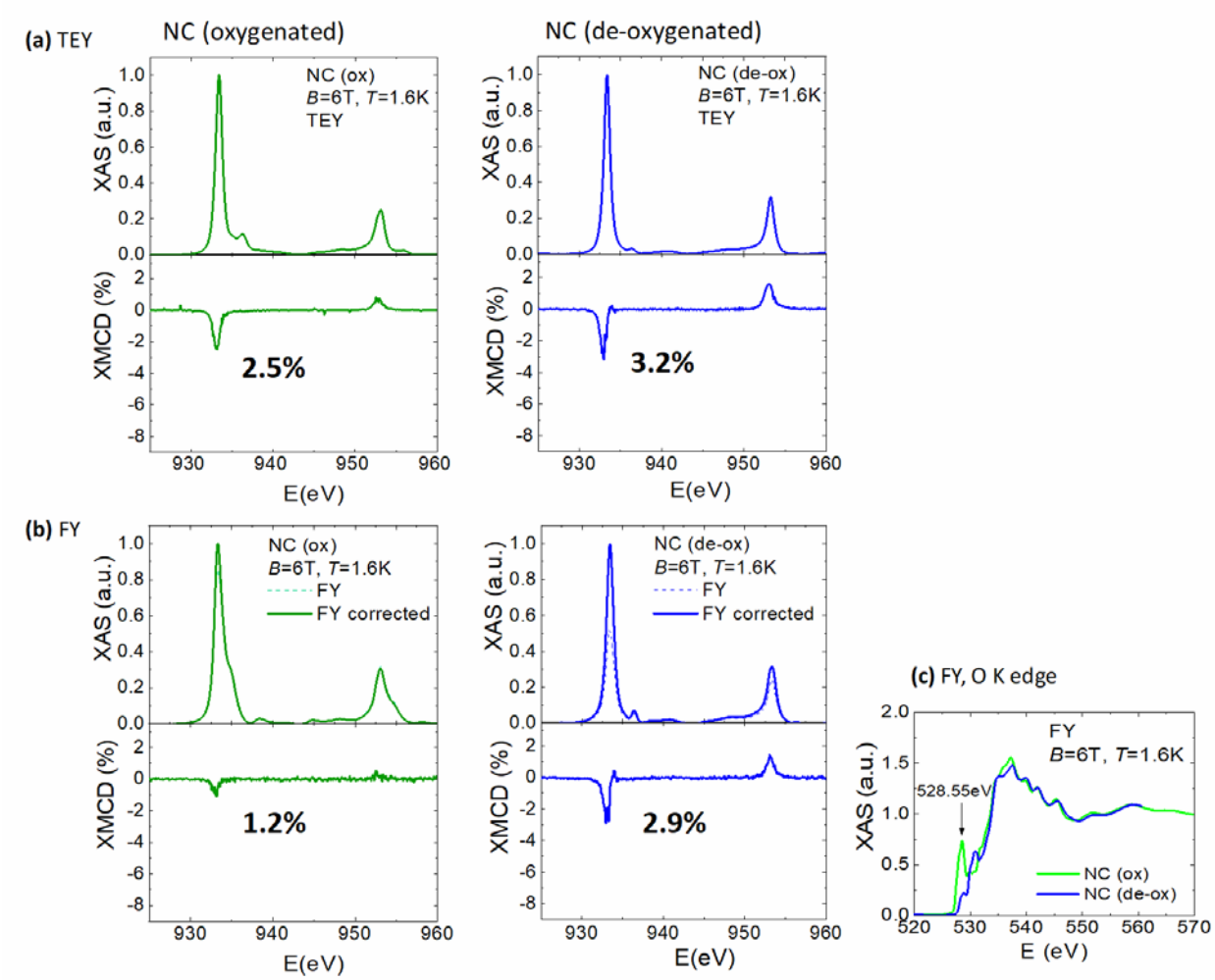

Figure 5. XAS & XMCD spectra at the Cu $L_{2,3}$ edge for (Left) a well oxygenated NC, and (Right) a different NC after des-oxygenation, measured simultaneously in TEY (a) and FY (b) at B=6 T, T=1.6 K and θ^*=55^o beam incidence angle; (c) XAS spectrum at O K edge measured in FY for the oxygenated and de-oxygenated NCs.

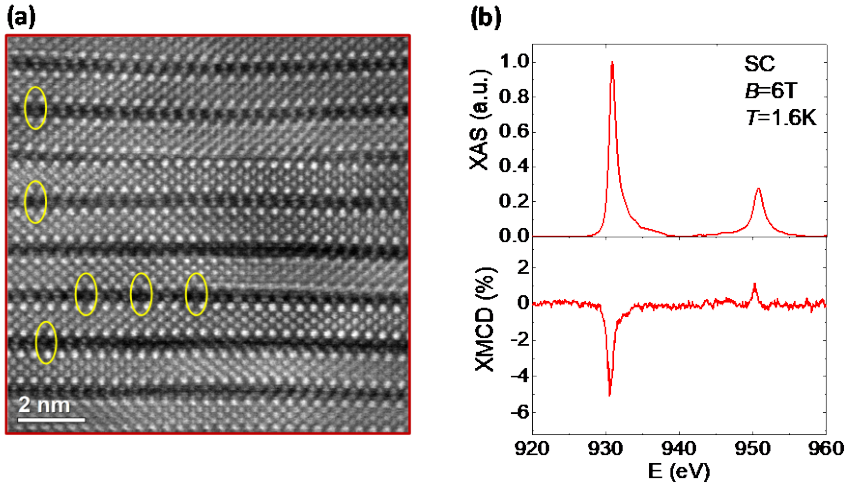

Figure 6. YBCO single-crystal: (a) rippled structure of Y124 intergrowths in the top-most part of the crystal (image corresponds to a zoom in the red square shown in Figure 2f). The circles signal the presence of cluster-vacancies; (b) XAS & XMCD spectra obtained in TEY (surface) mode at T=1.6 K, B=6 T and beam incidence angle θ=0^{o} .

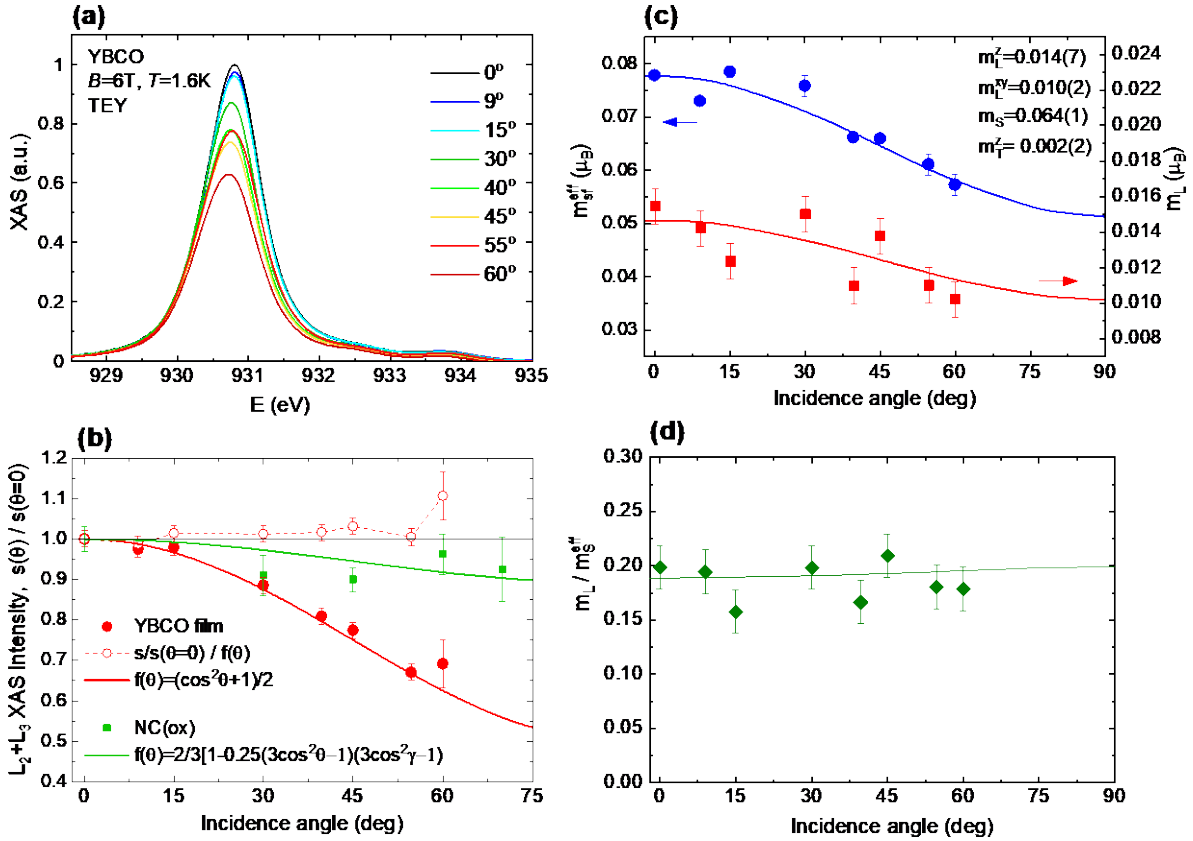

Figure 7 (a) Angular dependence of the L_3 XAS spectra, measured in TEY red at 6 T, 1.6 K for YBCO thin-film; (b) Integral of L_2+L_3 XAS spectra as a function of the incidence angle θ, normalized by the value at θ=0° (c) $m_L(\theta)$, $m_s^{eff}(\theta)$ and (d) $m_L/m_s^{eff}(\theta)$ ratio, determined and from angular-corrected sum rules at B=6 T, T=1.6 K for YBCO film (TEY). Lines are fits to Equations (9)-(10).

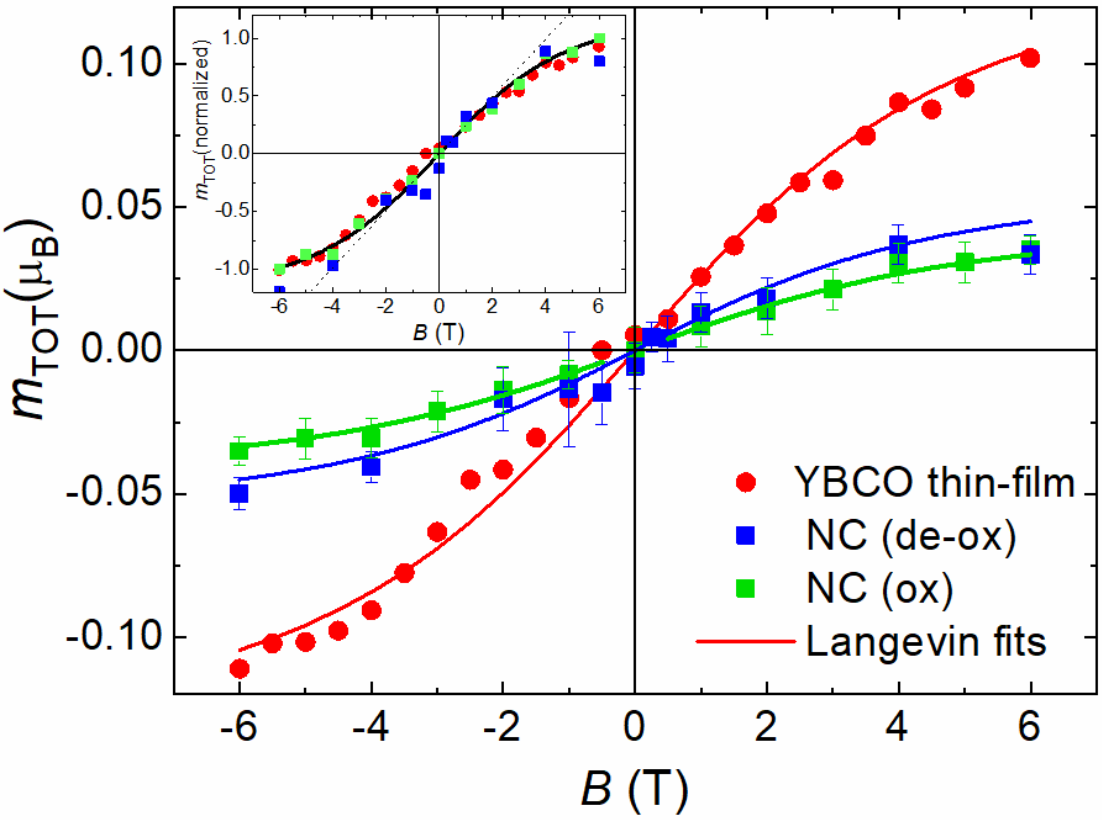

Figure 8. Magnetic-field dependence of the total magnetic moment (per average Cu in the sample), $m_{TOT}=m_S+m_L$, measured at T=1.6 K, θ=0° for the YBCO thin-film, the oxygenated and des-oxygenated NCs. The lines are fits to a Langevin function, with μ_C=1.18 μ_B, and μ_s=0.15(6) μ_B for YBCO thin-film, μ_s=0.05(1) μ_B for NC(ox) and μ_s=0.06(7) μ_B for NC(de-ox). Inset: curves normalized to a common saturation value collapse.

TABLES

Table 1. Orbital, effective spin and total magnetic moments, and orbital-to-effective moment ratio determined at T=1.6 K, B=6 T for the YBCO thin-film.

Measurement mode	m_L (μ_B)	m_s^{eff} (μ_B)	m_{TOT} (μ_B)	m_L/m_s^{eff}
TEY(Surface)	0.0183	0.113	0.1313	0.162
FY (Bulk)	0.0008	0.025	0.0258	0.032

AUTHOR INFORMATION

Corresponding Author

* Elena Bartolomé; Escola Universitària Salesiana de Sarrià (EUSS), Passeig Joan Bosco, 74; 08017 Barcelona, Spain. E-mail: ebartolome@euss.es

Present Addresses

†Now with Carl Zeiss SMT GmbH, SMT-ETRC, 73447-Oberkochen, Germany.

ACKNOWLEDGMENTS

We thank G. Nieva from *Centro Atómico de Bariloche* for YBCO single-crystal supply, and S. Hartman and R. Mishra from Oak Ridge National Lab for discussions on DFT simulations. We acknowledge financial support from Spanish Ministry of Economy and Competitiveness through the "Severo Ochoa" Programme for Centres of Excellence in R&D (SEV-2015-0496), COACHSUPERENERGY (MAT2014-51778-C2-1-R), SUMATE project RTI2018-095853-B-C21, co-financed by the European Regional Development Fund, COST-Nanohybri CA16218, DWARFS project (MAT2017-83468-R) and Catalan Government with 2017-SGR-1519. The XMCD experiments were performed at the BOREAS beamline of the ALBA Synchrotron Light Facility with the collaboration of ALBA staff. The STEM microscopy work was conducted in "Laboratorio de Microscopias Avanzadas" at the Instituto de Nanociencia de Aragon-Universidad de Zaragoza. Authors acknowledge the LMA-INA for offering access to their instruments and expertise. STEM-EELS analysis was conducted at the Center for Nanophase Materials Sciences, which is a DOE Office of Science User Facility. J.G. also acknowledges the Ramón y Cajal program (RYC-2012-11709).

REFERENCES

(1) *Superconductivity: From Materials Science to Practical Applications*; Mele, P., Prassides, K., Tarantini, C., Palau, A., Badica, P., Jha, A. K., Endo, T., Eds.; Springer Nature

Switzerland, 2019.

(2) MacManus-Driscoll, J. L.; Foltyn, S. R.; Jia, Q. X.; Wang, H.; Serquis, A.; Civale, L.; Maiorov, B.; Hawley, M. E.; Maley, M. P.; Peterson, D. E. Strongly Enhanced Current Densities in Superconducting Coated Conductors of $YBa_2Cu_3O_{7-x}$ + $BaZrO_3$. *Nat. Mater.* **2004**, *3*, 439–443.

(3) Kang, S.; Goyal, A.; Li, J.; Thompson, R.; AA, G.; Goyal, A.; Li, J. J.; Gapud, A. A.; Martin, P. M.; Heatherly, L.; Thompson, J. R.; Christen, D. K.; List, F. A.; Paranthaman, M.; Lee, D. F. High-Performance High-Tc Superconducting Wires. *Science.***2006**, *311*, 1911–1914.

(4) Shiohara, Y.; Taneda, T.; Yoshizumi, M. Overview of Materials and Power Applications of Coated Conductors Project. *Jpn. J. Appl. Phys.* **2012**, *51*, 010007-16.

(5) Malozemoff, A. P. Second-Generation High-Temperature Superconductor Wires for the Electric Power Grid. *Annu. Rev. Mater. Res.* **2012**, *42*, 373–397.

(6) Palau, A.; Valles, F.; Rouco, V.; Coll, M.; Li, Z.; Pop, C.; Mundet, B.; Gazquez, J.; Guzman, R.; Gutierrez, J.; Obradors, X.; Puig, T. Disentangling Vortex Pinning Landscape in Chemical Solution Deposited Superconducting $YBa_2Cu_3O_{7-x}$ Films and Nanocomposites. *Supercond. Sci. Technol.* **2018**, *31*, 034004-12.

(7) MacManus-Driscoll, J. L.; Zerrer, P.; Wang, H.; Yang, H.; Yoon, J.; Fouchet, A.; Yu, R.; Blamire, M. G.; Jia, Q. Strain Control and Spontaneous Phase Ordering in Vertical Nanocomposite Heteroepitaxial Thin Films. *Nat. Mater.* **2008**, *7*, 314-320.

(8) Maiorov, B.; Baily, S. A.; Zhou, H.; Ugurlu, O.; Kennison, J. A.; Dowden, P. C.;

Holesinger, T. G.; Foltyn, S. R.; Civale, L. Synergetic Combination of Different Types of Defect to Optimize Pinning Landscape Using $BaZrO_3$-Doped $YBa_2Cu_3O_7$. *Nat. Mater.* **2009**, *8*, 398-404.

(9) Matsumoto, K.; Mele, P. Artificial Pinning Center Technology to Enhance Vortex Pinning in YBCO Coated Conductors. *Supercond. Sci. Technol.* **2010**, *23*, 014001-12.

(10) Selvamanickam, V.; Chen, Y.; Shi, T.; Liu, Y.; Khatri, N. D.; Liu, J.; Yao, Y.; Xiong, X.; Lei, C.; Soloveichik, S.; Galstyan, E.; Majkic, G. Enhanced Critical Currents in $(Gd,Y)Ba_2Cu_3O_x$ Superconducting Tapes with High Levels of Zr Addition. *Supercond. Sci. Technol.* **2013**, *26*, 035006-9.

(11) Llordés, A.; Palau, A.; Gázquez, J.; Coll, M.; Vlad, R.; Pomar, A.; Arbiol, J.; Guzmán, R.; Ye, S.; Rouco, V.; Sandiumenge, F.; Ricart, S.; Puig, T.; Varela, M.; Chateigner, D.; Vanacken, J.; Gutiérrez, J.; Moshchalkov, V.; Deutscher, G.; Magén, C.; Obradors, X. Nanoscale Strain-Induced Pair Suppression as a Vortex-Pinning Mechanism in High-Temperature Superconductors. *Nat. Mater.* **2012**, *11*, 329–336.

(12) Gutiérrez, J.; Llordés, A.; Gázquez, J.; Gibert, M.; Romà, N.; Ricart, S.; Pomar, A.; Sandiumenge, F.; Mestres, N.; Puig, T.; Obradors, X. Strong Isotropic Flux Pinning in Solution-Derived $YBa_2Cu_3O_{7-x}$ Nanocomposite Superconductor Films. *Nat. Mater.* **2007**, *6*, 367–373.

(13) Obradors, X.; Puig, T.; Ricart, S.; Coll, M.; Gazquez, J.; Palau, A.; Granados, X. Growth, Nanostructure and Vortex Pinning in Superconducting $YBa_2Cu_3O_7$ Thin Films Based on Trifluoroacetate Solutions. *Supercond. Sci. Technol.* **2012**, *25*, 123001-32.

(14) Ziliang, L.; Coll, M.; Mundet, B.; Chamorro, N.; Vallès, F.; Palau, A.; Gázquez, J.; Ricart, S.; Puig, T.; Obradors, X. Control of Nanostructure and Pinning Properties in Solution Deposited $YBa_2Cu_3O_{7-x}$ Nanocomposites with Preformed Perovskite Nanoparticles. *Sci. Rep.* **2019**, *9*, 5828-14.

(15) Guzmán, R.; Gázquez, J.; Mundet, B.; Coll, M.; Obradors, X.; Puig, T. Probing Localized Strain in Solution-Derived $YBa_2Cu_3O_{7-\delta}$ Nanocomposite Thin Films. *Phys. Rev. Mater*. **2017**, *1*, 024801-7.

(16) Gázquez, J.; Guzmán, R.; Mishra, R.; Bartolomé, E.; Salafranca, J.; Magén, C.; Varela, M.; Coll, M.; Valvidares, S. M.; Gargiani, P.; Pellegrin, E.; Herrero-Martín, J.; Pennycook, S. J.; Pantelides, S. T.; Puig, T.; Obradors, X. Emerging Diluted Ferromagnetism in High-T_c Superconductors Driven by Point Defect Clusters. *Adv. Sci.* **2016**, *3*, 1500295-8.

(17) van der Laan, G.; Figueroa, A. I. X-Ray Magnetic Circular Dichroism - A Versatile Tool to Study Magnetism. *Coord. Chem. Rev.* **2014**, *277-278*, 95–129.

(18) De Luca, G. M.; Ghiringhelli, G.; Moretti Sala, M.; Di Matteo, S.; Haverkort, M. W.; Berger, H.; Bisogni, V.; Cezar, J. C.; Brookes, N. B.; Salluzzo, M. Weak Magnetism in Insulating and Superconducting Cuprates. *Phys. Rev. B.* **2010**, *82*, 214504-6.

(19) Coll, M.; Guzmán, R.; Garcés, P.; Gázquez, J.; Rouco, V.; Palau, A.; Ye, S.; Magén, C.; Suo, H.; Castro, H.; Puig, T.; Obradors, X. Size-Controlled Spontaneously Segregated Ba2YTaO6 Nanoparticles in $YBa_2Cu_3O_7$ Nanocomposites Obtained by Chemical Solution Deposition. *Supercond. Sci. Technol.* **2014**, *27*, 044008-9.

(20) Li, Z.; Coll, M.; Mundet, B.; Palau, A.; Puig, T.; Obradors, X. Accelerated Growth by Flash Heating of High Critical Current Trifluoroacetate Solution Derived Epitaxial Superconducting $YBa_2Cu_3O_7$ Films. *J. Mater. Chem. C* **2019**, *7*, 4748–4759.

(21) De La Cruz, F.; López, D.; Nieva, G. Thermally Induced Change in the Vortex Dimensionality of $YBa_2Cu_3O_7$ Single Crystals. *Philos. Mag. B* **1994**, *70*, 773–786.

(22) de Groot, F.M.F., *Personal communication*.

(23) Cuartero, V.; Lafuerza, S.; Subias, G.; Garcia, J.; Schierle, E.; Blasco, J.; Herrero-Albillos, J. X-Ray Magnetic Circular Dichroism Study of the Magnetic Anisotropy on $TbMnO_3$. *Phys. Rev. B* **2015**, *91*, 1–8.

(24) Troger, L.; Arvanitis, D.; Baberschke, K.; Michaelis, H.; Grimm, U.; Zschech, E. Full Correction of the Self-Absorption in Soft-Fluorescence Extended x-Ray-Absorption Fine Structure. *Phys. Rev. B* **1992**, *46*, 3283-3289.

(25) Gauquelin, N.; Hawthorn, D. G.; Sawatzky, G. A.; Liang, R. X.; Bonn, D. A.; Hardy, W. N.; Botton, G. A. Atomic Scale Real-Space Mapping of Holes in $YBa_2Cu_3O_{6+\delta}$. *Nat. Commun.* **2014**, *5*, 4275-7.

(26) Pennycook, P. D.; Nellist, S. J. *Scanning Transmission Electron Microscopy*; New York, 2011.

(27) Mundet, B. Atomic-Scale Characterization of Structural Distortions in Perovskite Oxide Thin Films, Institut de Ciència de Materials de Barcelona (ICMAB), University Autonoma of Barcelona, 2018.

(28) Tranquada, J. M.; Heald, S. M.; Moodenbaugh, A. R.; Xu, Y. Mixed Valency, Hole

Concentration, and T_c in $YBa_2Cu_3O_{6+x}$. *Phys. Rev. B* **1988**, *38*, 8893–8899.

(29) Grioni, M.; Van Acker, J. F.; Czyayk, M. T.; Fuggle, J. C. Unoccupied Electronic Structure and Core-Hole Effects in the x-Ray-Absorption Spectra of Cu_2O. *Phys. Rev. B* **1992**, *45*, 3309–3318.

(30) Hawthorn, D. G.; Shen, K. M.; Geck, J.; Peets, D. C.; Wadati, H.; Okamoto, J.; Huang, S. W.; Huang, D. J.; Lin, H. J.; Denlinger, J. D.; Liang, R.; Bonn, D. A.; Hardy, W. N.; Sawatzky, G. A. Resonant Elastic Soft X-Ray Scattering in Oxygen-Ordered $YBa_2Cu_3O_{6+\delta}$. *Phys. Rev. B.* **2011**, *84*, 075125-10.

(31) Li, Z.; Coll, M.; Mundet, B.; Chamorro, N.; Vallès, F.; Palau, A.; Gazquez, J.; Ricart, S.; Puig, T.; Obradors, X. *Submitted for publication.*

(32) Bartolomé, E.; Cayado, P.; Solano, E.; Mocuta, C.; Ricart, S.; Mundet, B.; Coll, M.; Gázquez, J.; Meledin, A.; van Tendeloo, G.; Valvidares, S.M.; Herrero-Martín, J.; Gargiani, P.; Pellegrin, E.; Magén, C.; Puig, T.; Obradors, O. Hybrid $YBa_2Cu_3O_7$ Superconducting-Ferromagnetic Nanocomposite Thin Films Prepared from Colloidal Chemical Solutions. *Adv. Electron. Mater.* **2017**, *3*, 1700037-11.

(33) Prajapat, C. L.; Singh, S.; Bhattacharya, D.; Ravikumar, G.; Basu, S.; Mattauch, S.; Zheng, J.-G.; Aoki, T.; Paul, A. Proximity Effects across Oxide-Interfaces of Superconductor-Insulator-Ferromagnet Hybrid Heterostructure. *Sci. Rep.* **2018**, *8*, 3732-15.

(34) Prada, R. de A.; Gaina, R.; Biškup, N.; Varela, M.; Stahn, J.; Bernhard, C. Controlling the

Strength of Ferromagnetic Order in $YBa_2Cu_3O_7/La_{2/3}Ca_{1/3}MnO_3$ Multilayers. *Phys. Rev. B* **2019**, *100*, 115129-14.

(35) Ivanov, Y. P.; Soltan, S.; Albrecht, J.; Goering, E.; Schütz, G.; Zhang, Z.; Chuvilin, A. The Route to Supercurrent Transparent Ferromagnetic Barriers in Superconducting Matrix. *ACS Nano* **2019**, *13*, 5655–5661.

(36) Zhang, H.; Gauquelin, N.; Botton, G. A.; Wei, J. Y. T. Attenuation of Superconductivity in Manganite/Cuprate Heterostructures by Epitaxially-Induced CuO Intergrowths. *Appl. Phys. Lett.* **2013**, *103*, 052606-4.

(37) Li, L. Ferroelectric/Superconductor Heterostructures. *Mater. Sci. Eng. R Reports* **2000**, *29*, 153–181.

(38) Stöhr, J.; König, H. Determination of Spin- and Orbital-Moment Anisotropies in Transition Metals by Angle-Dependent X-Ray Magnetic Circular Dichroism. *Phys. Rev. Lett.* **1995**, *75*, 3748–3751.

(39) Stepanow, S.; Mugarza, A.; Ceballos, G.; Moras, P.; Cezar, J. C.; Carbone, C.; Gambardella, P. Giant Spin and Orbital Moment Anisotropies of a Cu-Phthalocyanine Monolayer. *Phys. Rev. B.* **2010**, *82*, 014405-8.

(40) Piamonteze, C.; Miedema, P.; De Groot, F. M. F. Accuracy of the Spin Sum Rule in XMCD for the Transition-Metal L Edges from Manganese to Copper. *Phys. Rev. B.* **2009**, *80*, 184410-12.

(41) Thole, B.; Carra, P.; Sette, F.; van der Laan, G. X-Ray Circular Dichroism as a Probe of Orbital Magnetization. *Phys. Rev. Lett.* **1992**, *68*, 1943–1946.

(42) Carra, P.; Thole, B. T.; Altarelli, M.; Wang, X. X-Ray Circular-Dichroism and Local Magnetic-Fields. *Phys. Rev. Lett.* **1993**, *70*, 694–697.

(43) Stöhr, J.; Outka, D. A. Determination of Molecular Orientations on Surfaces from the Angular Dependence of Near-Edge x-Ray-Absorption Fine-Structure Spectra. *Phys. Rev. B.* **1987**, *36*, 7891–7905.

(44) Stepanow, S.; Honolka, J.; Gambardella, P.; Vitali, L.; Abdurakhmanova, N.; Tseng, T. C.; Rauschenbach, S.; Tait, S. L.; Sessi, V.; Klyatskaya, S.; Ruben, M.; Kern, K. Spin and Orbital Magnetic Moment Anisotropies of Monodispersed Bis(Phthalocyaninato)Terbium on a Copper Surface. *J. Am. Chem. Soc.* **2010**, *132*, 11900–11901.

(45) van der Laan, G. Relation between the Angular Dependence of Magnetic X-Ray Dichroism and Anisotropic Ground-State Moments. *Phys. Rev. B* **1998**, *57*, 5250–5258.

(46) Bartolomé, J.; Bartolomé, F.; García, L. M.; Filoti, G.; Gredig, T.; Colesniuc, C. N.; Schuller, I. K.; Cezar, J. C. Highly Unquenched Orbital Moment in Textured Fe-Phthalocyanine Thin Films. *Phys. Rev. B.* **2010**, *81*, 195405-8.

(47) Gargiani, P.; Rossi, G.; Biagi, R.; Corradini, V.; Pedio, M.; Fortuna, S.; Calzolari, A.; Fabris, S.; Cezar, J. C.; Brookes, N. B.; Betti, M. G. Spin and Orbital Configuration of Metal Phthalocyanine Chains Assembled on the Au(110) Surface. *Phys. Rev. B.* **2013**, *87*, 165407-11.

(48) Klanke, J.; Rentschler, E.; Medjanik, K.; Kutnyakhov, D.; Schönhense, G.; Krasnikov, S.; Shvets, I. V.; Schuppler, S.; Nagel, P.; Merz, M.; Elmers, H. J. Beyond the Heisenberg Model: Anisotropic Exchange Interaction between a Cu-Tetraazaporphyrin Monolayer

and Fe_3O_4(100). *Phys. Rev. Lett.* **2013**, *110*, 137202-5.

(49) Pennycook, S. J.; Jesson, D. E. High-Resolution Z-Contrast Imaging of Crystals. *Ultramicroscopy* **1991**, *37*, 14–38.

(50) Barla, A.; Nicolas, J.; Cocco, S.; Valvidares, M.; Herrero-Martín, J.; Gargiani, P.; Moldes, J.; Ruget, C.; Pellegrin, E.; Ferrer, S. Design and Performance of BOREAS, the Beamline for Resonant X-Ray Absorption and Scattering Experiments at the ALBA Synchrotron Light Source. *J. Synchrotron Radiat.* **2016**, *23*, 1507–1517.

GRAPHICAL ABSTRACT